Xu et al. *Microsystems & Nanoengineering* (2025)11:225
https://doi.org/10.1038/s41378-025-00989-1

Microsystems & Nanoengineering
www.nature.com/micronano

ARTICLE Open Access

Alleviating optical pumping inhomogeneity using a polarization-encoded metasurface in NMR co-magnetometers

Yan Xu[1,2,3,4,5], Zhen Chai[1,2,3,4,5]✉, Mingke Jin[6]✉, Rui Wang[1,2,3,4,5], Siyu Dai[1,2,3,4,5], Jing Qin[1,2,3,4,5] and Jianli Li[1,2,3,4,5]✉

Abstract

In nuclear magnetic resonance (NMR) co-magnetometers, the non-uniform transverse energy distribution of the pumping Gaussian beam can result in substantial optical pumping inhomogeneity and decoherence of atomic spins, which hinder the improvement of the precision and sensitivity of the sensor. One of the most significant recent technological advances for laser beam homogenization is the utilization of the microlens array system. However, the homogenized characteristics of the microlens array system vary with the propagation distance of the pumping light and are not suitable for chip integration, which will affect the sensitivity and compactness of the NMR system. To solve this issue, a metasurface homogenizer is demonstrated for encoding intensity information into the polarization profile of an incident Gaussian beam by combining the geometric phase and Malus' law with the transverse intensity distribution independent of the propagation distance. Compared to Gaussian beam pumping at identical input power, the metasurface homogenizer enhances the measured optical magnetic sensitivity by 23%. The proposed metasurface homogenizer not only realizes the higher precision and sensitivity in NMR co-magnetometers, but also highlights how metasurface-based technologies can contribute to the integrated quantum sensing regime.

Introduction

The nuclear magnetic resonance (NMR) co-magnetometer is constituted by a coupled spin ensemble of alkali metal atoms and inert gas nucleons. Based on a highly sensitive atomic magnetometer, it utilizes two inert gas nucleons with distinct gyromagnetic ratios to sense and suppress errors resulting from magnetic field fluctuations in the common mode, thereby making it a sensitive sensor of rotational angular velocity[1]. In an NMR system, the pumping light with the designed wavelength can polarize alkali metal electrons, and the electrons pass through spin-exchange hyperpolarized inert gas nucleons[2], which has significant applications in inertial measurement[3–5], geophysical research[6], and biological neural activity monitoring[7,8].

Uniformity in magnetic-optical systems is one of the key factors influencing resolution. Several studies have addressed the challenges in magnetic resonance by improving magnetic field uniformity, thus achieving better magnetic resonance results[9–11]. In most NMR co-magnetometer systems, the transverse light intensity of the pumping beam typically follows a Gaussian distribution with the maximum light intensity at the center, decreasing radially outward. However, the non-uniform transverse energy distribution of the pumping beam will inevitably lead to optical pumping inhomogeneity and atomic spin decoherence[12,13], and further restrains the improvement of the sensitivity of atomic sensors[14–17]. To eliminate the uneven polarization caused by the pumping light, it is significant to shape the Gaussian beam into a flat-topped beam[13,18]. Currently, numerous types of optical field homogenization methods, such as diaphragm interception[19], aspherical lens group[20,21], microlens array[22,23], top-hat diffractive optical element (DOE)[24],

Correspondence: Zhen Chai (zhenchai@buaa.edu.cn) or Mingke Jin (jinmingke@westlake.edu.cn) or Jianli Li (lijianli@buaa.edu.cn)
[1]Key Laboratory of Ultra-Weak Magnetic Field Measurement Technology, Ministry of Education, School of Instrumentation and Optoelectronic Engineering, Beihang University, Beijing 100191, China
[2]Institute of Large-scale Scientific Facility and Centre for Zero Magnetic Field Science, Beihang University, Beijing 100191, China
Full list of author information is available at the end of the article

spatial light modulator (SLM) homogenization[13,25,26], and beam integrator[27]. Although these methods have made some progress in different application scenarios, they each have their own limitations. While microlens arrays and DOEs can achieve beam homogenization at the micron scale through geometric optics principles, such as refraction or diffraction, their performance is often related to the propagation distance. Specifically, to achieve a uniform light intensity distribution, these methods require a fixed propagation distance to realize beam overlap or interference patterns. This requirement may adversely affect the polarization quality of the atomic ensemble in three-dimensional space, thus impacting the sensitivity of the sensor. Moreover, the use of additional collimating elements further increases the system's volume and complexity. In contrast, SLMs offer significant advantages in terms of real-time adjustability and flexibility. However, their relatively large volume makes it more challenging to integrate them into chip-level atomic sensors. Additionally, SLMs have the drawback of additional power consumption, and their refresh rate may affect the stability and continuous operation of atomic sensors. Therefore, although some beam shapers currently exist, they suffer from issues such as large volume, difficulty in integration, and poor performance, which limit their effectiveness in light field homogenization for practical applications. With the increasing demand for high-precision on-chip NMR co-magnetometers[28–30], it is a major issue to develop a miniaturized and easy-to-integrate optical field homogenizer for alleviating optical pumping inhomogeneity.

Recent advancements in metasurfaces have enabled the design of spatial distributions for amplitude[31,32], phase[33], and polarization[34] at subwavelength scales, facilitating the development of a wide variety of ultrathin devices with abnormal optical properties[35–37]. For instance, many functional components such as lenses, polarizers, modulators, and detectors have already used metamaterials as independent structures and achieved integration with various materials and devices to implement these functions[38]. Compared to traditional beam shapers, metasurfaces not only enable subwavelength optical operations with superior control precision but also, due to their planar structure, offer higher chip integration potential compared to the curved structures of microlenses and DOEs. This makes them particularly suitable for applications where volume is sensitive. Additionally, the passive nature of metasurfaces eliminates the power consumption and refresh rate limitations associated with SLMs, giving them a clear advantage in atomic sensor applications that require stable, continuous operation. This is a key factor in enhancing sensor sensitivity. Some studies show that metasurfaces have been particularly effective in controlling light intensities and homogenization. One of the metasurface-based strategies for obtaining a flat-top beam is achieved by modulating the spatial phase distribution of the incident Gaussian beam[39]. However, this method can produce a divergent output beam and require an extended propagation distance, rendering it unsuitable for integrated optical systems. Another method obtains the homogenized Gaussian beam at the focal plane of the metasurface based on the theory of geometric transformations[40], significantly reducing the beam spot size but altering the propagation angle, which limits its application in collimated optical paths.

In this paper, we propose a polarization-encoded metasurface homogenization strategy that maintains beam collimation while enabling easy integration. Based on Malus' law and the geometrical phase, a dielectric metasurface is employed to encode the intensity information into the polarization profile of an incident Gaussian beam, and the homogenized characteristics of the transmitted light remain consistent regardless of propagation distance. Our approach successfully facilitates the homogenization and collimation of the Gaussian beam. As shown in Fig. 1, the incident linearly polarized Gaussian light is transformed into homogenized light by the combination of a dielectric metasurface and an analyzer, subsequently converted to circularly polarized light by a quarter-wave plate (QWP) before the atomic vapor cell. The proposed metasurface homogenizer not only can achieve effective optical field homogenization and enhance the precision and sensitivity of the NMR co-magnetometer, but also underscores the potential of metasurface technologies in advancing integrated quantum sensing applications, characterized by a compact structure and seamless on-chip integration for both NMR co-magnetometers and other atomic sensing devices.

Results and discussion

Principle and design

The interaction between light and atomic ensembles in an NMR co-magnetometer can be effectively modeled and analyzed by using the Bloch-Torrey equations (SI Section 1). Figure 2a, b illustrate the spatial distribution of electron polarization in a cubic vapor cell with an inner diameter of 3 mm under the incidence of both Gaussian and homogenized light pumping. For the Gaussian beam scheme, the uneven light distribution results in regions of both over-polarization and under-polarization, and marked inhomogeneity in electronic polarization within the x-y plane. This disparity adversely affects the overall performance of the system and restricts the polarization transfer efficiency between alkali metal atoms and inert gas nuclei. In addition, the homogeneity of the pumping beam is crucial for enhancing the quality of atomic polarization, as it minimizes the discrepancies caused by variations in light intensity. The improvement in polarization distribution enhances the coupling between the

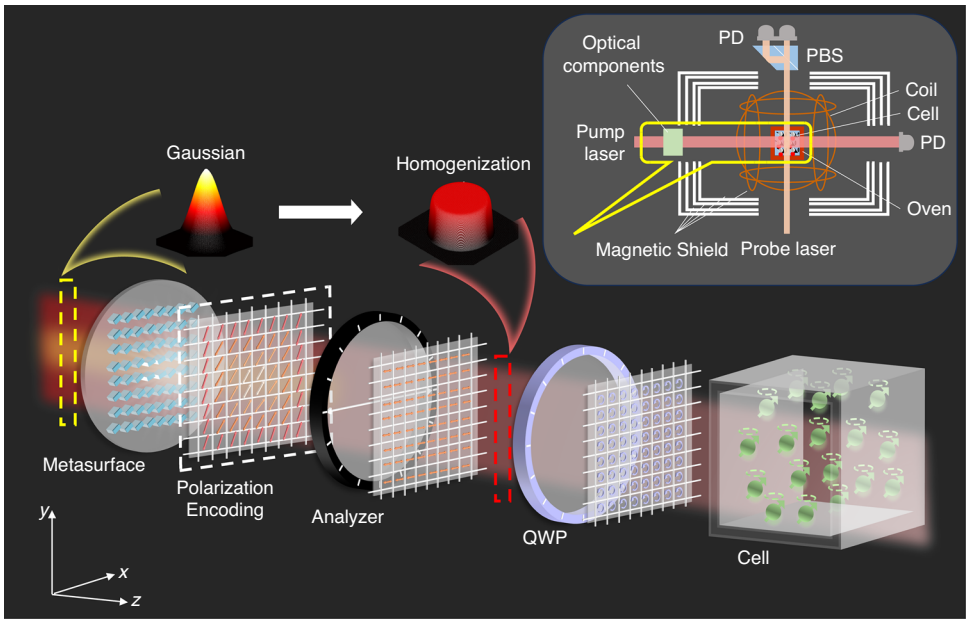

Fig. 1 Schematic diagram of the beam homogenization method based on polarization-encoded metasurface. QWP quarter-wave plate, PD photoelectric detection. The inset in the upper right corner illustrates the NMR co-magnetometer configuration implemented using this approach

spins of the alkali atoms and the inert gas nuclei, which contributes to the improvement of the sensor accuracy. Therefore, optimizing the beam profile is essential for achieving efficient polarization processes.

To achieve a homogenized beam, we calculated the intensity difference between the target output plane and the known input plane based on the principle of energy conservation. The ratio of the transverse two-dimensional optical field of the homogenized beam to the transmitted intensity of the input Gaussian beam is given by:

$$k_1(x,y) = \frac{I_2(x,y)}{I_1(x,y)} \tag{1}$$

where x and y are the coordinates on the beam plane, $I_1(x,y)$ is the input Gaussian beam, $I_2(x,y)$ is the output homogenized beam, and k_1 has a size between 0 and 1.

According to Malus' law and the optical intensity modulation mechanism (SI Section 2), the angle θ between the optical vibration direction of linearly polarized light on the target output plane and the optical vibration direction of linearly polarized light on the input plane is:

$$\theta(x,y) = \arccos\sqrt{\frac{I_2(x,y)}{I_1(x,y)}} = \arccos\sqrt{k_1(x,y)} \tag{2}$$

For any given two-dimensional planar coordinate, the corresponding $\theta(x,y)$ can be calculated to determine the two-dimensional polarization encoding strategy required for the homogenized optical field. To achieve polarization encoding of the beam at the micro-nanoscale, we employed rectangular meta-atoms as the fundamental polarization encoding elements, facilitating control over optical intensity. When incident circularly polarized light interacts with these rectangular meta-atoms, the scattered light contains a component of circular polarization that opposes the chirality of the incident light and introduces a phase factor related to the rotation angle of the meta-atoms, termed the geometric phase[41]. Under illumination by right-handed circularly polarized (RCP) or left-handed circularly polarized (LCP) light on the rectangular meta-atoms, the electric field expressions for the scattered light, as derived from Jones matrix theory, are given by[42]:

$$E_{\text{out}}^{R/L} = \frac{t_o + t_e}{2}E_i^{R/L} + \frac{t_o - t_e}{2}\exp(\mp i \cdot 2\varphi)E_i^{L/R} \tag{3}$$

where t_o and t_e represent the complex scattering coefficients of light along the fast and slow axes of the meta-atom, respectively, and φ is the spatial orientation angle of the meta-atom. The transmitted light consists of two components: the first is co-directed circularly polarized light with a modulation amplitude of $\frac{t_o+t_e}{2}$; the second is orthogonal circularly polarized light with a modulation amplitude of $\frac{t_o-t_e}{2}$ and a phase factor of 2φ. This additional phase factor, defined as $\phi = \pm 2\varphi$, indicates the phase shift sign under LCP or RCP light incidence conditions, allowing

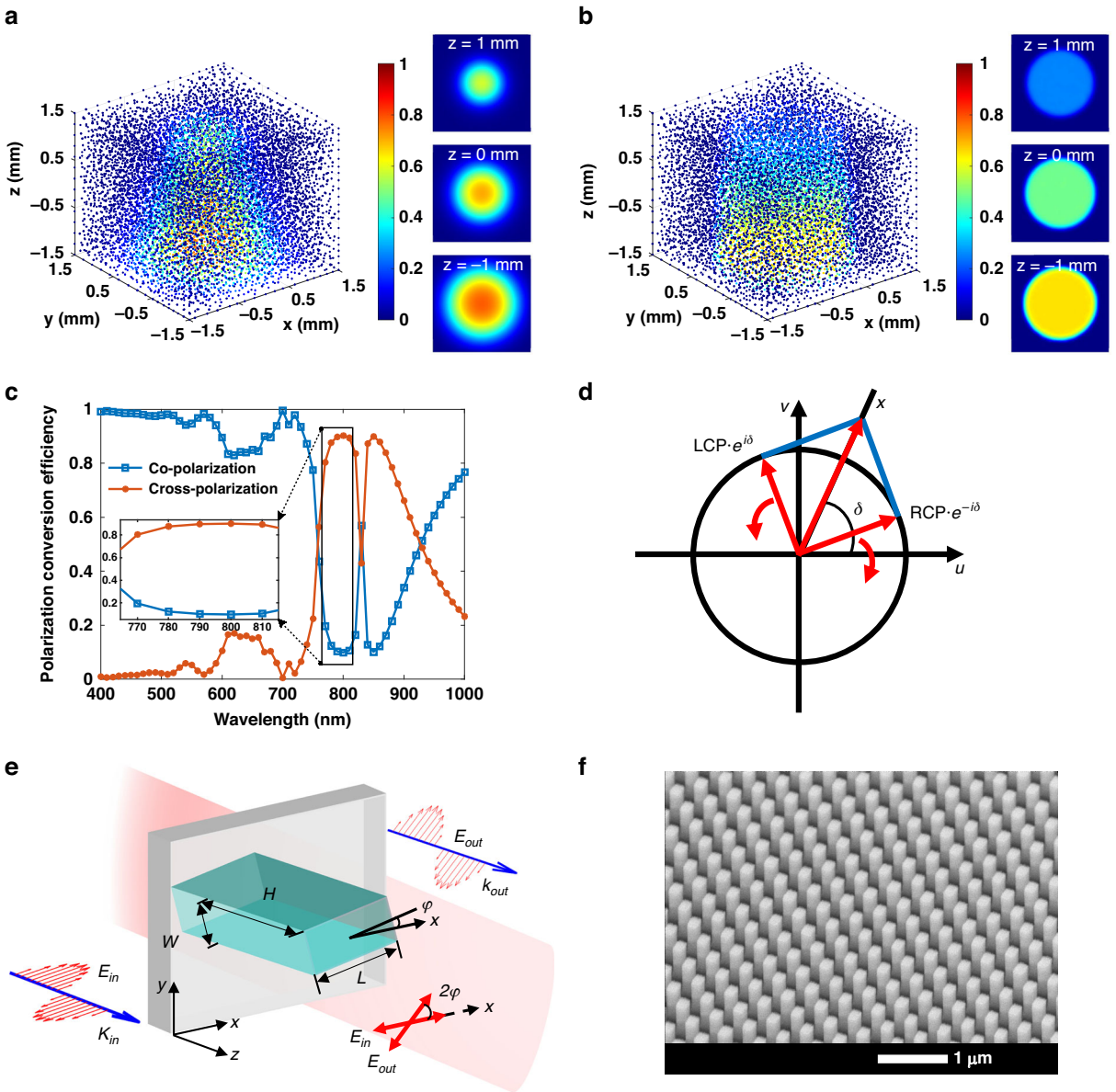

Fig. 2 Design of metasurface homogenizer. The spatial distribution of electron polarization rate in the cubic vapor cell under the pumping of **a** Gaussian light and **b** homogenized light, with cross-sectional intensity profiles at $z = -1$, 0, and 1 mm shown on the right; **c** the calculated polarization conversion efficiency of Si meta-atom set to be 190 nm (length) × 120 nm (width) × 620 nm (height) with the period of 370 nm; **d** linear polarization results from the coherent superposition of two plane circularly polarized light beams with opposite handedness and same propagation direction; **e** under the illumination of linear polarized light, the transmitted light is still linear polarized light and introduce an phase of 2φ; **f** a side-view SEM image of the central region of the metasurface

for continuous modulation of the incident light phase from 0 to 2π by adjusting the spatial orientation angle of the anisotropic meta-atoms.

The dielectric metasurface consists of a layer of spatially variant Silicon (Si) meta-atoms, which can efficiently convert the circularly incident light into the transmitted wave with opposite spin state. The proportion of circularly polarized light in the transmitted beam that opposes the chirality of the incident circularly polarized light is referred to as the cross-polarization conversion efficiency[43]. And the geometrical parameters of the Si meta-atoms are optimized at the designed wavelength of 795 nm of the D1 line for Rb (SI Section 3). Figure 2c shows that the geometrical parameters of the Si meta-atoms optimized to be 190 nm (length) × 120 nm (width) × 620 nm (height) with the meta-atom spacing $P = 370$ nm can achieve high cross-polarization conversion efficiency at 795 nm.

For a linearly polarized beam oriented along the x-axis, it can be regarded as a superposition of LCP and RCP with equal amplitude and an initial phase difference of 0, as illustrated in Fig. 2d. Under the illumination of RCP light onto a meta-atom with rotation angle of φ, the electric field of the transmitted LCP component can be described as $E_1 = e^{-i\cdot 2\varphi}\frac{1}{\sqrt{2}}\begin{bmatrix}1\\ i\end{bmatrix}$; Similarly, the electric filed of the transmitted RCP component with the incident of LCP is $E_2 = e^{+i\cdot 2\varphi}\frac{1}{\sqrt{2}}\begin{bmatrix}1\\ -i\end{bmatrix}$. Thus, the total electric field for the transmitted light is:

$$E_{\text{out}} = E_1 + E_2 = \frac{e^{-i\cdot 2\varphi}}{\sqrt{2}}\begin{bmatrix}1\\ i\end{bmatrix} + \frac{e^{i\cdot 2\varphi}}{\sqrt{2}}\begin{bmatrix}1\\ -i\end{bmatrix} = \sqrt{2}\begin{pmatrix}1\\ i\end{pmatrix}\begin{bmatrix}\cos 2\varphi\\ \sin 2\varphi\end{bmatrix} \tag{4}$$

Equation 4 indicates that the transmitted light retains linear polarization light with its polarization angle of 2φ. As shown in Fig. 2e, the linear polarization direction of the beam undergoes a counterclockwise rotation of 2φ after passing through a meta-atom with the rotation angle of φ.

The rectangular meta-atoms are arranged periodically in the x-y plane, with the spatial orientation angle defined as $\varphi(x,y) = \frac{1}{2}\theta(x,y)$, where each position corresponds to a specific polarization state $\theta(x,y)$ (SI Section 4). Thus, the metasurface can effectively transform the intensity-uneven Gaussian beam into an output beam exhibiting the desired encoded polarization states.

The polarization-encoded optical field homogenizer for atomic sensors comprises a dielectric metasurface and an analyzer aligned with the initial polarization direction of the laser. The analyzer selectively transmits light based on its polarization, thereby smoothing intensity variations and eliminating non-uniform light distribution, resulting in a homogeneous intensity across the x-y plane. The QWP converts the homogenized linearly polarized beam into circularly polarized light, facilitating the pumping of atomic ensembles within the atomic sensor vapor cell. We fabricated the Si metasurface with a diameter of 4 mm on a silicon dioxide substrate with a thickness of 500 μm by using electron beam lithography (EBL) process (SI Section 5). Figure 2f presents a side-view scanning electron microscopy (SEM) image of the central region of the metasurface.

The optical properties of the metasurface homogenizer

To visualize the intensity distribution of both the input and output beams, a beam profiler (Thorlabs BC207VIS) was employed to measure the light intensity distribution of the pumping Gaussian beam and the homogenized beam, as illustrated in Fig. 3a. The incident beam is a collimated Gaussian beam with a diameter of 3.4 mm, and the diameter of the homogenized spot is designed as 2.3 mm, corresponding to an intensity level of 40% above the peak. Figure 3b illustrates the simulation and measured two-dimensional intensity distributions of the Gaussian beam and the homogenized beam in the x-y plane. Figure 3c shows the corresponding intensity profiles along the x-axis. These results affirm the efficacy of the polarization-encoded homogenization scheme, achieving a notable degree of uniformity. To quantitatively evaluate the spatial intensity distribution characteristics and the uniformity of the homogenized output beam, we employed beam flux contrast as a metric. This contrast serves as a comprehensive descriptor of light intensity distribution, and the lower values indicate better uniformity (SI Section 6). Specifically, the flux contrasts for the Gaussian beam and the homogenized beam were 0.51917 and 0.28837 with standard deviations of 45.7153 and 31.6265. The power utilization efficiency is defined as the ratio of the output light power before and after passing through the homogenization device. Simulation calculations predict that the diameter of the output homogenized beam spot is 67.6% of the incident Gaussian beam diameter, yielding a predicted power utilization efficiency of 36.67%. This prediction is rooted in the optical properties of Gaussian beams, which are characterized by their specific intensity distribution and the behavior of light as they interact with the metasurface homogenizer. Experimentally, we measured an efficiency of 32.97%, showing good agreement with simulations while revealing a modest 3.7% discrepancy. This minor difference can be attributed to practical considerations including fabrication tolerances (SI Section 5), inherent substrate reflections from the 500 μm fused silica substrate, and slight deviations from ideal Gaussian beam profiles as shown in Fig. 3c. These experimental factors, typical in nanophotonic device implementation, explain the observed efficiency difference while maintaining results within expected tolerances, with theory and experiment showing excellent agreement.

The metasurface encodes intensity information into the polarization profile of the incident Gaussian beam, establishing a one-to-one correspondence between the original polarization direction and its spatial position following encoding. To elucidate the relationship between light intensity uniformity and the orientations of the metasurface and the analyzer's polarization axis, we demonstrated the alignment conditions among the incident beam's polarization direction, the metasurface orientation, and the analyzer's polarization axis. Since the homogenization effect of the metasurface depends on the precise alignment among the components of each part, we ensure precise alignment through measures such as mechanical structure and optical path alignment. By systematically changing the angles between these components, we observe periodic changes in

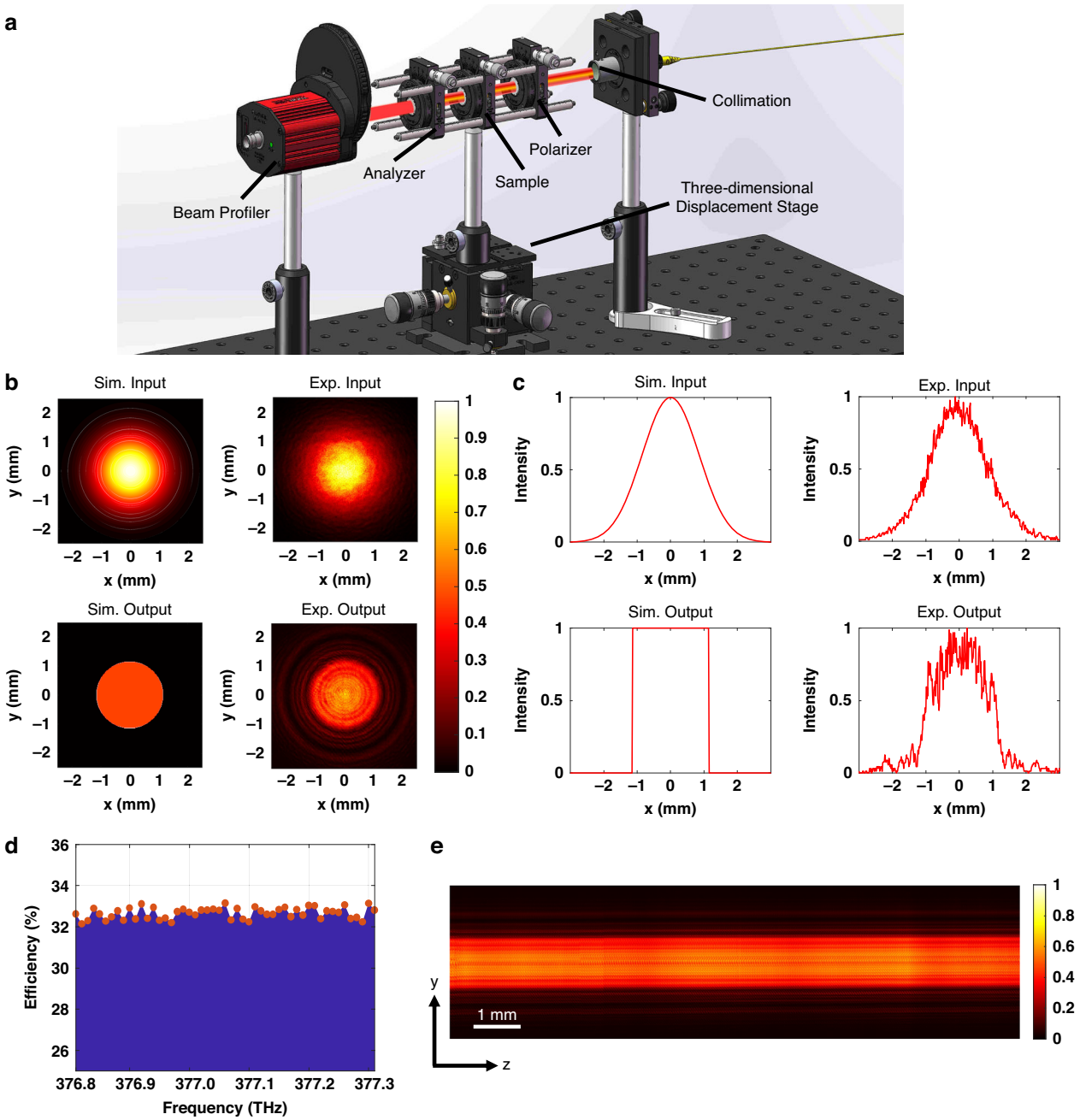

Fig. 3 The optical properties of the metasurface homogenizer. **a** The experimental setup; **b** simulation and measured intensity distributions of the input Gaussian beam and the output homogenized beam in the *x*-*y* plane; **c** simulation and measured intensity distributions of the input Gaussian beam and the output homogenized beam along the *x*-axis; **d** power utilization efficiency across various frequencies; **e** the propagation properties of the homogenized beam with a propagation length of 12 mm in free space

the output beam profile (SI Section 7). When the polarization axis of either the polarization-encoded metasurface or the analyzer is misaligned with the incident polarized light, insufficient homogenization or complete failure of the homogenization process may occur. Adjustments can be made by rotating either the polarization-encoded metasurface or the analyzer. Additionally, the designed metasurface device operates effectively within a defined tuning frequency range near the pumping light frequency for the NMR co-magnetometer. Figure 3d summarizes the power utilization efficiency test results across various frequencies, with efficiencies consistently around 33%. A distinctive feature of this method is its ability to accomplish beam homogenization while maintaining collimated

propagation. We further characterized the homogenization properties in free space at different propagation distances with a measurement interval of 0.05 mm. Figure 3e illustrates the axial propagation of the output beam over a distance of 12 mm in free space, maintaining good collimation and stable homogenization effects over sufficiently long distances. The polarization-encoded metasurface only modifies the polarization angle of the beam without affecting its propagation direction. Therefore, the homogenized beam maintains highly collimated propagation (SI Section 8).

Experimental demonstration of the atomic signals from the NMR co-magnetometers

To evaluate the impact of polarization-encoded homogenization technology on the performance of NMR co-magnetometers, we utilized the Gaussian and homogenized beam for polarizing alkali metal electrons, and the spot diameter of the incident light is consistent with the light power. We compared the atomic polarizability and relaxation with a pumping power profile ranging from 0.5 to 4.5 mW. As illustrated in Fig. 4a, the measured electron amplitude response reveals that the homogenized pumping light significantly enhances the amplitude of the electron signal at the same pumping power. The electron amplitude response peaks when the radio frequency (RF) magnetic field frequency matches the electron Larmor frequency, and Fig. 4b illustrates the measured electron resonance amplitudes at different pumping powers. Under the pumping of the homogenized light, the electron response peak increased by approximately 8%–22%. At lower pumping powers, an increase in light power markedly enhances the electron resonance amplitude, and a further escalation in light power will result in a saturation of the electron resonance amplitude. In compact NMR co-magnetometers, nuclear spin magnetic moments are typically on the order of a few nT. To measure NMR signals, we employed an in situ atomic magnetometer based on Rb atomic electron paramagnetic resonance. The presence of spin-exchange hyperfine coupling factors facilitates the detection and amplification of nuclear resonance signals, enabling effective capture and analysis. The output of the in situ magnetometer is proportional to the polarization of Rb atoms, highlighting the critical role of high atomic spin polarization in achieving sensitive magnetic field measurements. Using the nuclear frequency shift method, we also measured electron spin polarizability, as shown in Fig. 4c. Figure 4d illustrates the scale factor of the in situ magnetometer with different light powers, showing the relationship between the magnetic field perceived by the atoms and the output signal. The findings indicate that the homogenized light beam can effectively increase the average electron polarizability and the scale factor, and both increase with the intensity of the pumping light. Polarized electrons engage in spin-exchange interactions with inert gas atoms, leading to hyperpolarization of the nuclei. These inert gas atoms serve as the primary sensitive species for inertial measurements in NMR co-magnetometers, with their polarizability directly correlated with the signal-to-noise ratio (SNR) of the co-magnetometer's measurements. Figure 4e shows the polarizability of ^{129}Xe and ^{131}Xe nuclei, both of which are significantly lower than the electron polarizability. With increasing light power, the rate of increase in nuclear polarization levels off, and the polarizability of ^{129}Xe is higher than ^{131}Xe, which can obtain in a stronger hyperpolarization signal. Compared to the Gaussian light, homogenized light pumping can effectively enhance the polarization rates of the atomic nuclei.

Another key parameter of atomic spin is the relaxation rate, defined as the inverse of the time required for atomic spin polarization to decay to 1/e of its initial value. A lower relaxation rate indicates better atomic spin coherence. The transverse relaxation rate Γ of inert gas atoms characterizes the relaxation of atomic spins in the plane perpendicular to the quantization axis, directly influencing the angle random walk (ARW) of NMR co-magnetometers[44]:

$$ARW = \frac{\Gamma}{SNR\sqrt{\Delta f}} \tag{5}$$

where Δf is the bandwidth of phase noise. It is evident that reducing the transverse relaxation rate of inert gas atoms can mitigate the ARW.

Given that ^{129}Xe nuclei generate a stronger signal, we focused on measuring its relaxation rate. Figure 4f shows the variation of the transverse relaxation rate of ^{129}Xe as a function of pumping power, indicating that an increase in pumping power correlates with an increase in the nuclear transverse relaxation rate and a corresponding decrease in atomic coherence. Considering the influence of pumping power on atomic polarization, achieving an optimal balance in the actual system is crucial to avoid either excessively low or high pumping power. When the pumping power is insufficient or excessive, atomic polarization may become saturated or inadequate, which results in a similar relaxation rate for both the homogenized beam and the Gaussian beam. However, in the optimal pumping power range from 1 to 4 mW, the homogenized light can significantly reduce the transverse relaxation rate of inert gas atoms. To quantitatively verify the effect of homogenized light, we calculated the variations of electron polarizability, nuclear polarizability, scaling factor, and nuclear relaxation rate under the pumping of the homogenized and Gaussian beam (SI

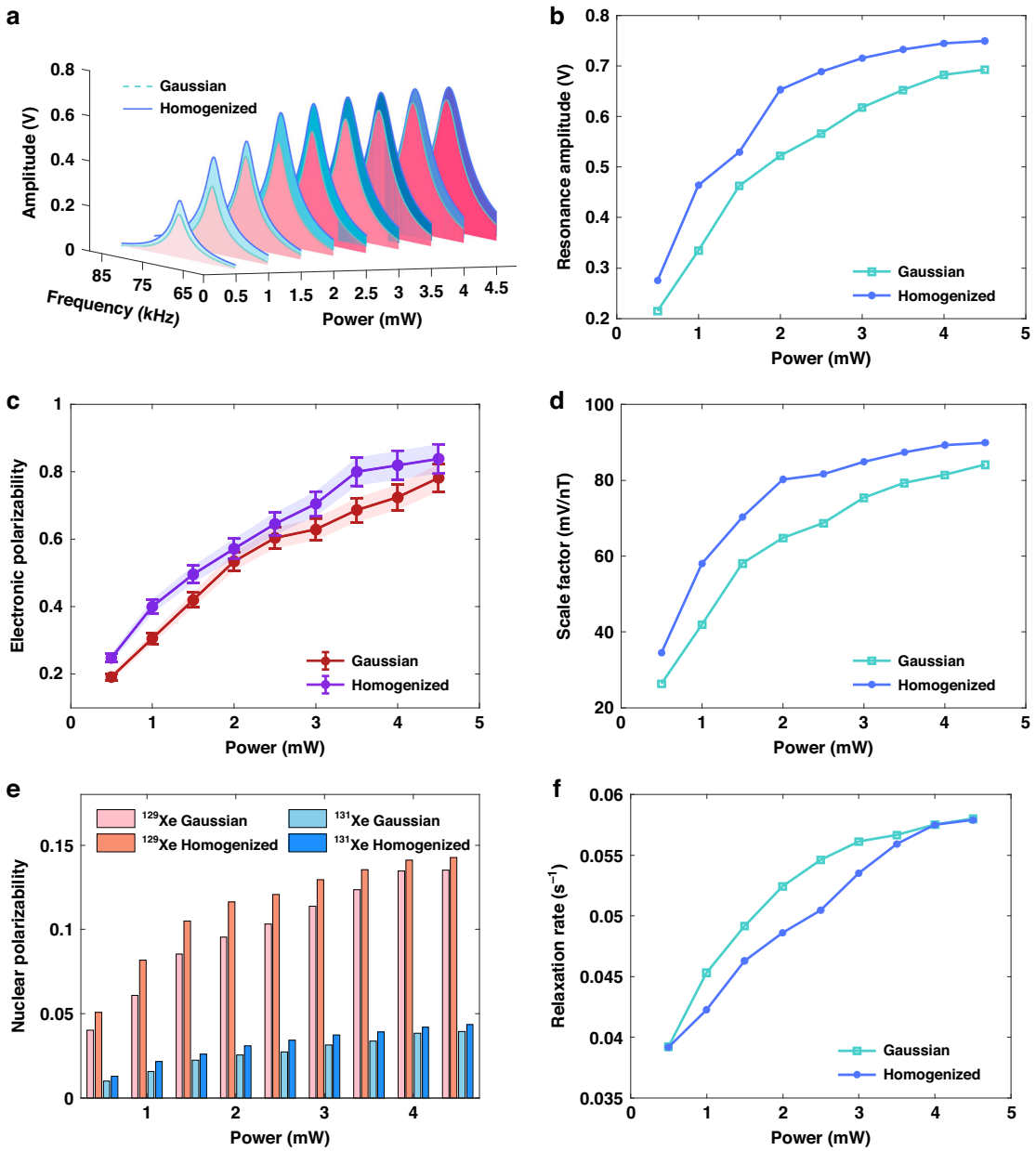

Fig. 4 Experimental results of atomic polarization and relaxation. **a** Electron amplitude-frequency response signals; **b** electron resonance amplitudes; **c** electron polarizability; **d** scale factor of the in situ magnetometer; **e** inert gas atomic polarizability; **f** transverse relaxation rate of ^{129}Xe

Section 9). Compared to Gaussian light, the homogenized light utilized for pumping can improve the electronic and nuclear polarization, as well as scaling factors, ranging from 5% to 40%. Additionally, enhancements are generally greater at lower pump powers than at higher pumping powers. These measurements collectively demonstrate that the homogenized beam effectively improves atomic polarization uniformity within the vapor cell space, providing robust validation of its performance.

The transverse relaxation rate of nuclei is influenced by various factors and can be described as follows[45,46]:

$$\Gamma = \Gamma_{coll} + \Gamma_{wall} + \Gamma' + \Gamma_{\Delta B} \tag{6}$$

where Γ_{coll} denotes the relaxation rate caused by collisions between inert gas nuclei and alkali metal atoms, which is directly proportional to the density of Rb. Γ_{wall} represents relaxation resulting from collisions with the vapor cell walls, and Γ' represents the gas-phase relaxation rate due

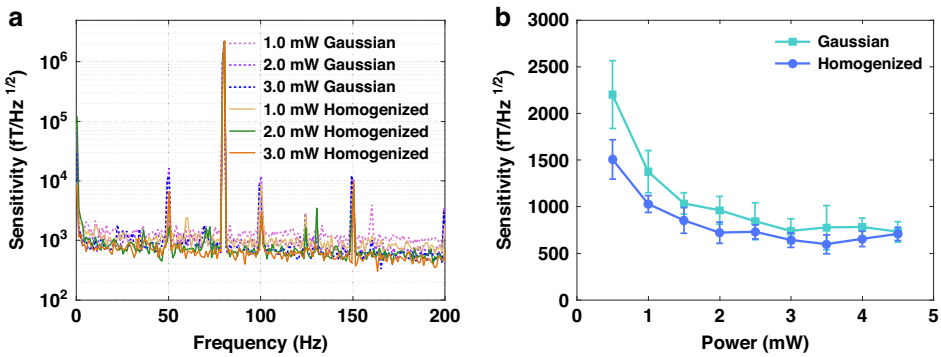

Fig. 5 Magnetic measurement sensitivity. **a** Sensitivity curves under Gaussian and homogenized light pumping schemes; **b** magnetic measurement sensitivity as a function of the varying pumping powers

to inert gas atom self-collisions, typically negligible compared to other influences in the NMR system. Additionally, $\Gamma_{\Delta B}$ describes the relaxation rate arising from magnetic field inhomogeneity. Under conditions of stable temperature within the vapor cell, the total transverse relaxation rate of the inert gas atoms can be approximated as[45]:

$$\Gamma \approx a\left(\frac{\partial B_z}{\partial l}\right)^2 + c \tag{7}$$

where $\frac{\partial B_z}{\partial l}$ denotes the first-order magnetic field gradient, and l refers to the distance along the x, y, or z axes. In a three-dimensional space, the inhomogeneity of the alkali metal vector magnetic field can be attributed to the uneven spatial distribution of electron spin polarization[17,47]. When electron polarization is inhomogeneous, the resultant inhomogeneity of the equivalent magnetic field can increase the relaxation rate of inert gas atoms.

To evaluate the magnitude of the magnetic field gradients in the three axial directions within the vapor cell, we incorporated a triaxial gradient magnetic field coil, with its symmetry center aligned with the center of the atomic cell (SI Section 10). The results indicate that the z-axis corresponds to the direction of the pumping light propagation, where absorption effects create a discernible magnetic field gradient. The lowest points on the relaxation rate measurement curves occur at nearly the same location, indicating minimal differences under the influence of the Gaussian and homogenized pumping light. In the x-y plane, the homogenized pumping light can reduce the magnetic field gradient within the cell compared to Gaussian light. Furthermore, the magnetic field gradient along the y-axis is somewhat larger than that along the x-axis, attributed to the y-direction aligning with the gas handle of the cell. During the blowing process of the cell, removal from the inflation tubing can easily lead to thermal deformation of the cell, resulting in the retention of a tail tube, which often fuses to form a gas handle. This can cause atomic diffusion into the handle space, consequently increasing the magnetic field gradient. Overall, these findings highlight the importance of understanding homogenized beams, especially in their role in reducing magnetic field gradients within atomic vapor cells. The transverse magnetic field gradient, which arises from the non-uniform polarization of atoms, is significantly mitigated by the use of homogenized pumping light.

Based on the fundamental principles of NMR co-magnetometer, the in situ atomic magnetometer is sensitive to nuclear spin precession, modulating the rotation angle of the probing light at the precession frequency, which is subsequently extracted using a phase-locked loop. To evaluate the overall performance of the NMR co-magnetometer, we conducted a spectral analysis of the output signals from the in situ magnetometer to obtain the sensitivity of the magnetic measurement. A calibration magnetic field with a frequency of 80 Hz and an amplitude of 2.3 nT was applied along the x-axis, and the magnetometer's response was recorded over approximately 20 s. The power spectral density of the response was calculated, averaged, and normalized against the frequency response to derive the noise spectral density. Figure 5a shows the measured sensitivity curves for three different pumping light powers at varying frequencies. Notably, the 50 Hz noise peak is attributable to power line interference, while other sharp noise peaks correspond to harmonics of the calibration magnetic field. The 50 Hz interference originates from the alternating current power line, which introduces a sinusoidal noise component into the measurement system. Since the co-magnetometer incorporates several core components, including optical, thermal, magnetic, and detection elements, all connected to the circuitry, various solutions can be implemented to mitigate these spikes. Potential measures include using metal shielding enclosures or shielded cables to cover sensitive

circuits and equipment, with a single-point grounding of the shielding layer. Furthermore, isolation transformers can be employed to block ground loop noise, or advanced filtering techniques can be incorporated into the signal processing to effectively suppress both the mains frequency and its harmonics in real-time. To further compare the sensitivity levels of the homogenized light with Gaussian light, we calculated the average values of eight points closely surrounding the calibration signal, providing a measure of the baseline noise level. Figure 5b details the magnetic measurement sensitivities at various operational points of the pumping light. At lower pumping light powers, the sensitivity becomes worse obviously; however, within the range of 2–4 mW, sensitivity levels remain similarly good. In the NMR co-magnetometer, when the pumping light power is low, the homogenized beam improves the uniformity of atomic polarization within the atomic vapor cell, thereby enhancing the sensitivity of the system. However, when the pumping light power is too high, atomic polarization within the cell may experience saturation effects. These saturation effects mask the improvement in beam uniformity provided by the homogenized beam, thereby reducing the advantage of the homogenized beam over the Gaussian beam. Additionally, as the light power increases, the sensitivity curves for both beams gradually stabilize. This occurs because, with increasing pump power, the signal strength increases, but noise also increases, causing the sensitivity to level off. Quantitative comparisons revealed that the application of homogenized pumping light can significantly enhance magnetic measurement sensitivity, further achieving a minimum sensitivity of approximately 600 fT/$Hz^{1/2}$ at 3.5 mW—an enhancement of 23% over the Gaussian light condition. This improvement effectively elevates the SNR of the resonant signal and enhances the overall performance of the sensor.

Conclusion

In summary, we have developed a miniaturized optical field homogenization scheme based on polarization-encoded metasurfaces, effectively addressing the issue of optical pumping non-uniformity caused by the inhomogeneous transverse energy distribution of Gaussian beams in conventional NMR co-magnetometers. A metasurface homogenizer is designed for encoding intensity information into the polarization profile of an incident Gaussian beam by combining the geometric phase and Malus' law with the transverse intensity distribution independent of the propagation distance, while overcoming the limitations of conventional homogenization techniques, which struggle to maintain uniformity during propagation and suffer from issues related to large volume and integration difficulties. Experimental results demonstrate that our proposed homogenization method significantly can obtain higher atomic polarization and lowers relaxation rates compared to traditional Gaussian light pumping configuration.Quantitative comparisons reveal that the utilization of uniform pumping light can markedly improve magnetic measurement sensitivity. When the pumping power is the same at 3.5 mW, the magnetic measurement sensitivity is increased by 23% relative to the Gaussian beam baseline.This study opens up new directions for the application of optical metasurfaces, which can greatly improve the for optical pumping homogenization system in atomic sensors. The method is compact and easy to integrate on the chip, highlighting its application potential in atomic sensor technologies such as on-chip NMR co-magnetometer, and illustrating the contribution of metasurface-based technologies to integrated quantum sensing systems. Looking ahead, structures with the same homogenization function have the potential to explore the use of single-layer metasurfaces to further simplify the design, reduce volume, and streamline the integration process, providing new pathways for compact and efficient integration in future atomic sensor applications.

Methods

Sample fabrication

Firstly, a double-polished fused silica substrate with a thickness of 500 μm was cleaned. A 620 nm thick a-Si thin film was deposited onto the substrate via the plasma-enhanced chemical vapor deposition process. Following this, the electron resist (ZEP520A) was spin-coated to a thickness of 200 nm onto the a-Si thin film and baked on a hotplate at 180 °C for 3 min. The resist was exposed using a JEOL JBX-9500FS EBL system with an exposure dose of 150 μC/cm² and an electron beam current of 2 nA at 100 kV. The exposed resist was developed to transfer the metasurface pattern. After that, the Cr hard mask layer was evaporated on top of the resist pattern by using the electron beam evaporation technique and immersed in the corresponding solution for the lift-off process. Finally, the a-Si thin film was etched by using an ICP etching system (OXFORD PlasmaPro 100 Cobra) with an etching rate of 10 nm/s, and the metasurface optical chip was obtained after the removal of the Cr hard layer and photoresist.

NMR co-magnetometer experimental setup

The experimental setup is illustrated in Fig. 6. The pumping light is emitted from a distributed Bragg reflector (DBR) semiconductor laser and coupled into a polarization-maintaining fiber (PMF). The pumping light is centered at the Rb D1 resonance wavelength and propagates along the *z*-axis. The optical path of the pumping light encompasses an adjustable collimator, a polarizing beam splitter (PBS), and a noise absorber (Thorlabs NEL03) to stabilize the optical intensity. Before entering

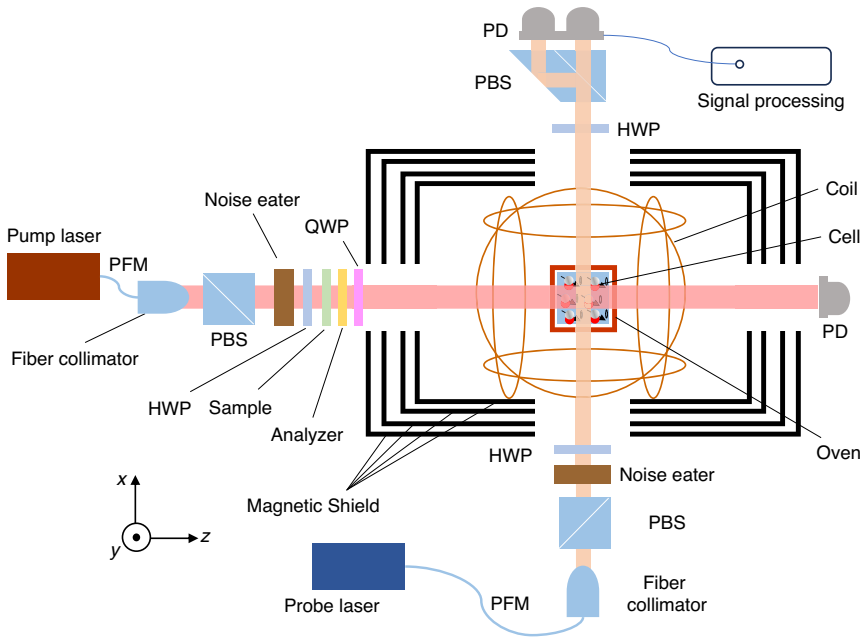

Fig. 6 NMR co-magnetometer experimental setup. PMF polarization-maintaining fiber, PBS polarization beam splitter, HWP half-wave plate, QWP quarter-wave plate

the vapor cell, the light subsequently passes through a metasurface and an analyzer, ultimately achieving circular polarization with a QWP. The vapor cell, fabricated from cubic glass with an inner diameter of 3 mm and an outer diameter of 4 mm, is encased within a four-layer magnetic shielding. Under typical conditions, the cell is filled with a drop of naturally abundant Rb atoms, along with 2 Torr of ^{129}Xe, 15 Torr of ^{131}Xe, 200 Torr of N_2 as a quenching gas, and 10 Torr of H_2 serving as a buffer gas. The vapor cell is heated to 120 °C by using two 220 kHz AC heaters located in a boron nitride ceramic oven, with temperature monitored via platinum resistors, which work in concert to maintain the desired thermal conditions. The probing light is also sourced from a DBR laser diode and is introduced into the vapor cell through PMF. This probing light propagates along the x-axis and utilizes optical components like those in the pumping light path. The wavelength of the probing light is tuned to the vicinity of the Rb D2 line, delivering approximately 1.6 mW of linearly polarized light. The probing signal is demodulated and processed through a balanced detector (Thorlabs PDB210A) and lock-in amplifiers to extract information regarding atomic spin dynamics. Additionally, a set of triaxial coils is integrated within the magnetic shielding, controlled by the lock-in amplifiers, and powered by a precision current source to generate the magnetic field while compensating for residual magnetic fields. A static bias magnetic field of $B_{z_0} = 10\ \mu T$ is applied along the z-axis to establish the quantization axis, with an RF magnetic field amplitude of $B_c = 6.4\ \mu T$. The RF magnetic field frequency ω_c, is in resonance with the Larmor frequency of Rb, while also applying a RF magnetic field along the x-axis, which resonates with the Larmor frequency of Xe.

Atomic polarization and relaxation rate measurement

To determine the magnitude of the electron polarizability, we transitioned the pumping light from σ^+ to σ^- and measured the frequency difference $\Delta\nu_{Xe}$ of the inert gas atoms' resonance before and after the transition. This yields the Rb electronic spin polarizability P_{Rb} which can be described as follows[48]:

$$\Delta\nu_{Xe} = 2\gamma_{Xe}B_{Rb} = 2\gamma_{Xe} \cdot \frac{2}{3}\kappa_0\mu_0\mu_B g_s n_{Rb} \cdot \frac{1}{2}P_{Rb} \qquad (8)$$

where γ_{Xe} is the gyromagnetic ratio of Xe, κ_0 is the enhancement factor of Rb-Xe, μ_0 is the permeability in free space, μ_B is the Bohr magnet, and g_s is the g-factor of the electron.

The spin polarizability and transverse relaxation time of the nucleons are measured by using the free induced decay (FID) method[49]. A π/2 pulse was applied along the x-axis in resonance with the magnetic field acting on the inert gas atoms, and the resulting FID signal was collected by a NI DAQ card. Given that the pumping light propagates along the z-axis, the spin magnetic moment of the inert gas atoms also aligns along this axis, with no projection in the x-y plane. When a magnetic field is present in the x-y plane, it will cause a deviation of the spin magnetic moment from the z-axis, leading to a projection

within the x-y plane that is subsequently reflected in the probe signal. We fitted the decay curve of the FID signal by using an exponential model $f = Ae^{-t/\tau}$ which can obtain the extraction of the transverse relaxation time and rate. The nuclear polarizability P_{Xe} can be calculated from the initial amplitude V_{FID} of the FID signal:

$$V_{\mathrm{FID}} = K \cdot B_{\mathrm{Xe}} = K \cdot \frac{2}{3}\kappa_0\mu_0\mu_{\mathrm{Xe}}n_{\mathrm{Xe}}P_{\mathrm{Xe}} \tag{9}$$

where μ_{Xe} is the magnetic moment of Xe, and K is the magnetometer scale factor obtained from the calibrated signal. n_{Xe} is the number density of Xe.

Acknowledgements
The authors appreciate the financial support from the Innovation Program for Quantum Science and Technology, 2021ZD0300403; National Natural Science Foundation of China, General Program, 62373028; Zhejiang Provincial Natural Science Foundation, LZ24F050007; National Science Fund for Distinguished Young Scholars, 62225102; Beijing Natural Science Foundation, General Program, 4232071; and National Natural Science Foundation of China, 42388101.

Author details
[1]Key Laboratory of Ultra-Weak Magnetic Field Measurement Technology, Ministry of Education, School of Instrumentation and Optoelectronic Engineering, Beihang University, Beijing 100191, China. [2]Institute of Large-scale Scientific Facility and Centre for Zero Magnetic Field Science, Beihang University, Beijing 100191, China. [3]National Institute of Extremely-Weak Magnetic Field Infrastructure, Hangzhou 370051, China. [4]Beihang Hangzhou Innovation Institute, Hangzhou 310052, China. [5]Hefei National Laboratory, Hefei 230088, China. [6]School of Engineering, Westlake University, Hangzhou 310024, China

Author contributions
Y.X., Z.C., M.K.J., and J.L.L. conceived and designed the idea. Y.X. and M.K.J. designed and characterized the metasurface with assistance from S.Y.D. and J.Q., and R.W. helped build the test system. Y.X. performed the test and analyzed the data. Y.X., Z.C., and M.K.J. wrote the manuscript with input from all authors. J.L.L. and Z.C. supervised the project.

Data availability
The authors declare that the data supporting the findings of this study are available with the paper and its Supplementary Information files. The data that support the findings of this study are available from the corresponding author upon reasonable request.

Conflict of interest
The authors declare no competing interests.

Supplementary information The online version contains supplementary material available at https://doi.org/10.1038/s41378-025-00989-1.

Received: 31 March 2025 Revised: 8 May 2025 Accepted: 26 May 2025
Published online: 24 November 2025

References

1. Jia, Y. et al. The effect of tensor light shift on residual magnetic field compensation in a nuclear spin co-magnetometer. *Appl. Phys. Lett.* **116**, 142405 (2020).
2. Terrano, W. A. & Romalis, M. V. Comagnetometer probes of dark matter and new physics. *Quantum Sci. Technol.* **7**, 014001 (2021).
3. Kornack, T. W., Ghosh, R. K. & Romalis, M. V. Nuclear spin gyroscope based on an atomic comagnetometer. *Phys. Rev. Lett.* **95**, 230801 (2005).
4. Wei, K. et al. Ultrasensitive atomic comagnetometer with enhanced nuclear spin coherence. *Phys. Rev. Lett.* **130**, 063201 (2023).
5. Zhang, K., Zhao, N. & Wang, Y.-H. Closed-loop nuclear magnetic resonance gyroscope based on Rb-Xe. *Sci. Rep.* **10**, 1–7 (2020).
6. Qiao, Z. et al. Zero- to ultralow-field nuclear magnetic resonance technology, principle and oil and gas detection method. *Prog. Geophys.* **38**, 709–719 (2023).
7. Weiskopf, N., Edwards, L. J., Helms, G., Mohammadi, S. & Kirilina, E. Quantitative magnetic resonance imaging of brain anatomy and in vivo histology. *Nat. Rev. Phys.* **3**, 570–588 (2021).
8. Bao, B., Hua, Y., Wang, R. & Li, D. Quantum-based magnetic field sensors for biosensing. *Adv. Quantum Technol.* **6**, 2200146 (2023).
9. Maurya, S. K. & Schmidt, R. Shaping the RF transmit field in 7T MRI using a nonuniform metasurface constructed of short conducting strips. *ACS Appl. Mater. Interfaces* **16**, 47284–47293 (2024).
10. Park, M., Noh, H. & Park, N. Mitigation of B1+ inhomogeneity for ultra-high-field magnetic resonance imaging: hybrid mode shaping with auxiliary EM potential. *Sci. Rep.* **10**, 11752 (2020).
11. Santini, T. et al. Improved 7 Tesla transmit field homogeneity with reduced electromagnetic power deposition using coupled Tic Tac Toe antennas. *Sci. Rep.* **11**, 3370 (2021).
12. Wu, Z., Chai, Z., Mao, Y., Tian, H. & Liu, Z. High-resolution optical magnetic resonance imaging of electronic spin polarization in miniaturized atomic sensors. *Appl. Phys. Lett.* **121**, 204103 (2022).
13. Chen, X. et al. Optimization of beam shaping for ultrasensitive inertial measurement using a phase-only spatial light modulator. *Appl. Opt.* **61**, C55–C64 (2022).
14. Pang, H. et al. Comprehensive analysis of the effects of magnetic field gradient on the performance of the SERF co-magnetometer. *Opt. Express* **31**, 5215–5228 (2023).
15. Yuan, L. et al. Measurement and analysis of polarization gradient relaxation in the atomic comagnetometer. *Measurement* **217**, 113043 (2023).
16. Wang, T., Peng, J., Liu, Z., Mao, Y. & Wang, X. Optical magnetic combination method for suppressing the Rb polarization-induced magnetic gradient in Rb-Xe NMR co-magnetometers. *Opt. Express* **31**, 17663–17676 (2023).
17. Wang, Z., Li, J. & Xiong, Z. Influence of pump beam truncation on transverse relaxation time of ^{129}Xe in a nuclear magnetic resonance gyroscope. *OSA Contin.* **3**, 903–910 (2020).
18. Jia, J. et al. Acoustic frequency atomic spin oscillator in the quantum regime. *Nat. Commun.* **14**, 6396 (2023).
19. Wu, C, Liu, R. & Xu, Y. Design and simulation of flat-top microstructure fiber. In *Proc. International Conference on Photonics and Optical Engineering (icPOE 2014)* Vol. 9449, 496–502 (SPIE, 2015).
20. Shi, G., Li, S., Huang, K., Yi, H. & Yang, J. Gaussian beam shaping based on aspheric cylindrical lenses. *Optoelectron. Lett.* **10**, 439–442 (2014).
21. Price, B. D., Lowry, S. N., Hartley, I. D. & Reid, M. Subterahertz refractive flat-top beam shaping via 3D printed aspheric lens combination. *Appl. Opt.* **59**, 5429–5436 (2020).
22. Homburg, O., Bayer, A., Mitra, T., Meinschien, J. & Aschke, L. Beam shaping of high power diode lasers benefits from asymmetrical refractive micro-lens arrays. In *Proc. High-Power Diode Laser Technology and Applications VI* Vol. 6876, 95–101 (SPIE, 2008).
23. Han, J. et al. Conversion of a Gaussian-distributed circular beam to a flat-top-distributed square beam in laser shock processing based on a micro-lens array structure. *Optik* **274**, 170525 (2023).
24. Nasrollahi, V. et al. Laser drilling with a top-hat beam of micro-scale high aspect ratio holes in silicon nitride. *J. Mater. Process. Technol.* **281**, 116636 (2020).
25. Ma, H. et al. Generation of flat-top beam with phase-only liquid crystal spatial light modulators. *J. Opt.* **12**, 045704 (2010).
26. Hendriks, A., Naidoo, D., Roux, F. S., López-Mariscal, C. & Forbes, A. The generation of flat-top beams by complex amplitude modulation with a phase-only spatial light modulator. In *Proc. Laser Beam Shaping XIII* Vol. 8490, 55–62 (SPIE, 2012).
27. Dickey, F. M. *Laser Beam Shaping: Theory and Techniques* 2nd edn (CRC Press, 2018).
28. Kitching, J. Chip-scale atomic devices. *Appl. Phys. Rev.* **5**, 031302 (2018).
29. Noor, R. M. & Shkel, A. M. MEMS components for NMR atomic sensors. *J. Microelectromech. Syst.* **27**, 1148–1159 (2018).
30. Jia, Y., Liu, Y., Chen, C. & Chen, R. Design of a multi-laser module for optical pumping in compact atomic gyroscopes. In *Proc. AOPC 2023: Laser Technology*

and Applications; and Optoelectronic Devices and Integration Vol. 12959, 29–38 (SPIE, 2023).
31. Bao, L. et al. Multi-beam forming and controls by metasurface with phase and amplitude modulations. *IEEE Trans. Antennas Propag.* **67**, 6680–6685 (2019).
32. Yue, Z. et al. Versatile polarization conversion and wavefront shaping based on fully phase-modulated metasurface with complex amplitude modulation. *Adv. Opt. Mater.* **10**, 2200733 (2022).
33. Chen, J. et al. From volumetric to planar multiplexing: phase-coded metasurfaces without the Bragg effect. *Adv. Mater.* **35**, 2304386 (2023).
34. Zang, X. et al. Polarization encoded color image embedded in a dielectric metasurface. *Adv. Mater.* **30**, 1707499 (2018).
35. Fu, P. et al. Metasurface enabled on-chip generation and manipulation of vector beams from vertical cavity surface-emitting lasers. *Adv. Mater.* **35**, 2204286 (2023).
36. Liu, W. et al. Metasurface enabled wide-angle Fourier lens. *Adv. Mater.* **30**, 1706368 (2018).
37. Zuo, J. et al. Chip-integrated full-stokes polarimetric imaging sensor. In *Proc. 2022 Conference on Lasers and Electro-Optics (CLEO)* 1–2 (IEEE, 2022).
38. Padilla, W. J. & Averitt, R. D. Imaging with metamaterials. *Nat. Rev. Phys.* **4**, 85–100 (2022).
39. Abbaszadeh, A., Ahmadi-Boroujeni, M. & Tehranian, A. A compact polarization insensitive all-dielectric metasurface lens for Gaussian to tophat beam shaping in sub-terahertz regime. *Opt. Commun.* **462**, 125313 (2020).
40. Zhang, X., Zhang, X., Duan, Y., Zhang, L. & Ni, X. All-optical geometric image transformations enabled by ultrathin metasurfaces. *Nat. Commun.* **14**, 8374 (2023).
41. Guo, Y. et al. Classical and generalized geometric phase in electromagnetic metasurfaces. *Photonics Insights* **1**, R03 (2022).
42. Ni, P.-N. et al. Spin-decoupling of vertical cavity surface-emitting lasers with complete phase modulation using on-chip integrated Jones matrix metasurfaces. *Nat. Commun.* **13**, 1–10 (2022).
43. Li, J., Yuan, Y., Wu, Q. & Zhang, K. Bi-isotropic Huygens' metasurface for polarization-insensitive cross-polarization conversion and wavefront manipulation. *IEEE Trans. Antennas Propag.* **72**, 2445–2454 (2024).
44. Zhong, G. et al. Measuring transverse relaxation time of xenon atoms based on single beam of laser in nuclear magnetic resonance gyroscope. *J. Shanghai Jiaotong Univ. Sci.* **28**, 569–576 (2023).
45. Liu, X., Chen, C., Qu, T., Yang, K. & Luo, H. Transverse spin relaxation and diffusion-constant measurements of spin-polarized 129Xe nuclei in the presence of a magnetic field gradient. *Sci. Rep.* **6**, 1–8 (2016).
46. Zhan, X. et al. Improved compensation and measurement of the magnetic gradients in an atomic vapor cell. *AIP Adv.* **10**, 045002 (2020).
47. Mao, Y., Dong, B., Li, J., Liu, Z. & Jie, S. Influence of pump power and beam diameter on the transverse relaxation rate of noble gas nuclear spins in the nuclear magnetic resonance gyroscope. In *Proc. SPIE-CLP Conference on Advanced Photonics 2022* **12601**, 157–162 (SPIE, 2023).
48. Liu, X. H., Luo, H., Qu, T. L., Yang, K. Y. & Ding, Z. C. Measuring the spin polarization of alkali-metal atoms using nuclear magnetic resonance frequency shifts of noble gases. *AIP Adv.* **5**, 107119 (2015).
49. Chen, L. et al. A method for measuring the spin polarization of 129Xe by using an atomic magnetometer. *AIP Adv.* **7**, 085221 (2017).